

Thermonuclear Supernovae: Simulations of the Deflagration Stage and Their Implications

V. N. Gamezo^{1*}, A. M. Khokhlov¹, E. S. Oran¹, A. Y. Chtchelkanova², R. O. Rosenberg³

¹Laboratory for Computational Physics and Fluid Dynamics,
Naval Research Laboratory, Washington, D.C. 20375, USA

²Strategic Analysis Inc., Arlington, VA 22201, USA

³Center for Computational Science,
Naval Research Laboratory, Washington, D.C. 20375, USA

*To whom correspondence should be addressed.
E-mail: gamezo@lcp.nrl.navy.mil

Science Express (online), November 21, 2002. To appear in *Science*, January 2003

Abstract

Large-scale three-dimensional numerical simulations of the deflagration stage of a thermonuclear supernova explosion show the formation and evolution of a highly convoluted turbulent flame in a gravitational field of an expanding carbon-oxygen white dwarf. The flame dynamics is dominated by the gravity-induced Rayleigh-Taylor instability that controls the burning rate. The thermonuclear deflagration releases enough energy to produce a healthy explosion. The turbulent flame, however, leaves large amounts of unburnt and partially burnt material near the star center, whereas observations imply these materials only in outer layers. This disagreement could be resolved if the deflagration triggers a detonation.

According to observations and models, many stars that steadily burn their nuclear fuel for millions or billions of years suddenly end their lives with a powerful explosion that produces a bright object called a supernova. A supernova explosion can be powered either by the gravitational energy released during the core collapse of a massive star, or by the nuclear energy released by explosive thermonuclear burning of a star. Here, we focus on thermonuclear supernovae that belong to the Type Ia (SN Ia) in the observation-based classification (1-3).

Thermonuclear supernovae are produced by explosions of white dwarfs (WD), small dense stars composed of carbon and oxygen nuclei and detached degenerate electrons (1,3-10). The term degenerate means that electrons occupy all possible quantum states below a certain energy. The hydrostatic equilibrium in a WD is supported for the most part by the degenerate-electron pressure that does not depend on temperature. White dwarfs form at the end of the evolution of stars whose original masses are less than 8 solar masses (M_{\odot}). A star can lose a large fraction of its material by ejecting outer layers into space at the final stages of evolution. The mass of a remaining WD is always less than the Chandrasekhar limit, $1.4M_{\odot}$, above which a hydrostatic equilibrium of degenerate matter is impossible. An isolated carbon-oxygen WD is stable and almost inert because its temperature is not high enough to induce any substantial nuclear reactions. This isolated dead star can exist almost indefinitely, slowly cooling down as it radiates its energy into space. Observations show, however, that more than 50% of all stars are not isolated. They belong to groups of two or more stars that orbit a common center of mass. In a close binary system, a WD can increase its own mass by accreting material from its companion star. Such systems are considered to be the most probable SN Ia progenitors, even though the exact nature of the companion star and the details of the mass accretion are still unclear (1,3-5,7-9).

When the mass of the WD approaches the Chandrasekhar limit, any small mass increase results in a substantial contraction of the star, and the material near its center is compressed. This increases the temperature and accelerates thermonuclear reactions near the center. The released energy further increases the temperature, thus further accelerating thermonuclear reactions. This process is slowed down by the neutrino, convective and conductive cooling. Nevertheless, the temperature in the WD center rises and reaches the point where the energy release overwhelms the energy outflow. In an ordinary non-degenerate star, the energy release would be stabilized by a thermal expansion accompanied by the work against gravity. In a WD, however, the initial temperature increase does not affect the degenerate-electron pressure, and, therefore, does not lead to any substantial expansion that could slow down thermonuclear reactions and prevent the runaway process. Eventually, the temperature increases to the level where the thermal and the degenerate-electron pressure components become comparable, and the material begins to expand. At that time, however, the expansion is already unable to quench the fast thermonuclear burning ignited in the center of a WD. The thermonuclear runaway mechanism in degenerate matter was first described in (11) and now is a key component of all plausible SN Ia scenarios (1,4-9). Depending on the scenario, the ignition may occur near the center, off center, or in outer layers of the star. Here, we consider the central ignition mode.

Ignition starts a SN Ia explosion that lasts only a few seconds, but releases $\simeq 10^{51}$ ergs, about as much energy as the Sun would radiate during 8 billion years. The energy is produced by a network of thermonuclear reactions that begins from ^{12}C and ^{16}O nuclei and ends in ^{56}Ni and other iron-group elements. Large amounts of intermediate-mass elements, such as Ne, Mg, Si, S, and Ca, are created as well. The main energy-producing reactions occur in a thin layer, called a thermonuclear flame, that propagates outwards. At the beginning, the flame is laminar and its propagation velocity is controlled by thermal conductivity. As the flame moves away from the center, it becomes turbulent and accelerates. Eventually, the burning can undergo a transition from a relatively slow, subsonic regime, called deflagration, into a supersonic regime, called detonation, where the reaction front is preceded by a shock wave. Most of the energy released during the explosion transforms into kinetic and thermal energies of the expanding material. When the sum of kinetic (E_k) and thermal (E_t) energies exceeds the potential energy of self-gravitation E_g , the star becomes unbound, such that expanding material is no longer bound by gravity and will continue to expand indefinitely.

Thermonuclear reactions that occur during the explosion provide energy for the expansion, but not for the luminosity of the expanding gas observed as a SN Ia. The energy source for the luminosity is the slow radioactive decay sequence $^{56}\text{Ni} \rightarrow ^{56}\text{Co} \rightarrow ^{56}\text{Fe}$. The luminosity reaches its maximum 15 to 20 days after the explosion, and then decreases slowly until all the ^{56}Co decays. The maximum brightness of a SN Ia is

comparable to the brightness of an entire galaxy, and can vary by an order of magnitude from one supernova to another. Observations also show that the maximum luminosity of SNe Ia in visible wavelengths correlates with the rate at which the luminosity decreases after the maximum (12-14). This and other approximate correlations summarized in (2,8) make it possible to use SNe Ia as standard candles to measure distances and estimate cosmological parameters critical for our understanding of the global evolution of the Universe (4,5,7-10,15-19).

The importance of SNe Ia as standard candles grows as observational techniques improve and estimations of cosmological parameters become more accurate. We are approaching the limit, however, where the reliance on empirical correlations becomes the main source of uncertainty. Even though the correlation between the maximum luminosity and rate of decrease of the luminosity for SNe Ia has a theoretical explanation (20) based on a one-dimensional model, this is at best only a first approximation that does not take into account a detailed explosion mechanism and its possible variations. The only way to solve this problem is to study details of supernova explosions using multidimensional numerical simulations.

One-dimensional (1D) numerical models have been extensively used to test general ideas about possible explosion mechanisms (21-24,4,6). Delayed-detonation models (25-32), that postulate a deflagration-to-detonation transition (DDT) at some stage of the thermonuclear explosion, are most successful in reproducing observed characteristics of SNe Ia. Many important details, however, including the mechanism of DDT, are still unknown because SN Ia explosions are intrinsically three-dimensional (3D) phenomena.

Only a full-scale 3D numerical model may be expected to reproduce all key features of the explosion that involves propagation of a turbulent thermonuclear flame in the gravitational field of a white dwarf. Building such a model is a complicated interdisciplinary problem on the leading edge of astrophysics, nuclear physics, combustion physics, and computational physics. Full-scale 3D numerical simulations of thermonuclear supernova explosions have become a reality during the last few years (33-35), in great part owing to the progress in computational technology. Here, we describe a 3D numerical model, present numerical results for the deflagration stage of the explosion, and discuss implications of the results for astrophysics of SNe Ia.

Physical and Numerical Model. The numerical model described in more detail in (36) is based on reactive Euler equations that represent mass, momentum, and energy conservation laws for an inviscid fluid. The thermodynamic properties of the fluid are defined by the equation of state of degenerate matter, which is well known from basic theory and includes contributions from ideal Fermi-Dirac electrons and positrons, equilibrium Planck radiation, and ideal ions. Reactions involved in the thermonuclear burning of the carbon-oxygen mixture are described by a simplified four-equation kinetic scheme (25,33). This kinetic scheme is coupled with a flame-capturing technique (37,33) that introduces an additional partial differential equation and ensures thermonuclear flame propagation at a prescribed speed S . The resulting set of equations is integrated on a Cartesian adaptive mesh using an explicit, second-order, Godunov-type numerical scheme (37,38). The mesh is dynamically refined around shock waves, flame fronts, and in regions of steep gradients of density, pressure, composition, and tangential velocity. The computational cell size dx varies within predefined limits dx_{min} and dx_{max} .

The large-scale simulations described here do not resolve the physical thickness of a flame that differs from the white dwarf radius R_{WD} by up to 12 orders of magnitude. Therefore, the flame speed must be provided by an additional subgrid model that takes into account physical processes at scales smaller than the computational cell size. We define the flame speed S as

$$S = \max(S_l, S_t), \quad (1)$$

where the steady-state laminar flame speed S_l in carbon-oxygen degenerate matter is a known function of temperature, density, and composition (39,40). The speed S_t of a quasi-steady-state turbulent flame driven by the gravity-induced Rayleigh-Taylor (RT) instability depends on the gravitational acceleration g and the length scale L (37,41):

$$S_t \simeq 0.5\sqrt{AgL} \quad (2)$$

where $A = (\rho_0 - \rho_1)/(\rho_0 + \rho_1)$ is the Atwood number, and ρ_0 and ρ_1 are the densities ahead and behind the flame front, respectively. The driving scale L is set equal to one or two computational cell sizes dx .

Equation (2) is based on the two main properties of a turbulent flame (37,41): self-similarity of the flame structure and self-regulation of the flame speed. Self-similarity means that the 3D distortions of the flame

surface at different scales are similar. Self-regulation means that changing the flame speed at small scales does not affect the flame speed at larger scales. This occurs because a higher flame speed at small scales causes small flame wrinkles to burn out, thus decreasing the flame surface. The resulting burning rate, defined as a product of the flame speed at small scales and the flame surface, does not change. This subgrid model makes it possible to reproduce the correct flame propagation in numerical simulations while explicitly resolving only the large-scale flame structure. If the resolved flame structure is self-similar and self-regulating, and behaves according to the Eq. (2), the subgrid model just extends this behavior to unresolved small scales. Shifting the boundary between resolved and unresolved scales by changing the numerical resolution should not affect the turbulent flame propagation. The solution obtained should then be independent of numerical resolution and on the exact value of S_t . Numerical convergence tests described in (36) show that for the high ($dx_{min} = 2.6 \times 10^5$ cm) and medium ($dx_{min} = 5.2 \times 10^5$ cm) numerical resolutions the 3D structure of the turbulent flame was resolved in sufficient detail to reproduce key dynamic properties of the flame included in the subgrid model. Changing L in Eq. (2) from dx to $2dx$ has only a minor effect on the converged solution. The results are self-consistent, reasonably accurate, and can be used to analyze explosion scenarios for thermonuclear supernovae.

Thermonuclear deflagration in carbon-oxygen white dwarf of Chandrasekhar mass. The initial conditions for the simulations (see (36) for more details) were set up for a Chandrasekhar-mass WD in hydrostatic equilibrium with the initial radius $R_{WD} = 2 \times 10^8$ cm, the initial central density $\rho_c = 2 \times 10^9$ g/cm³, the uniform initial temperature $T = 10^5$ K, and the uniform initial composition with equal mass fractions of ¹²C and ¹⁶O nuclei. The 3D computational mesh extended from the WD center $x = y = z = 0$ to $x = y = z = 2.6R_{WD}$. Thus, we model one octant of the WD assuming mirror symmetry along the $x = 0$, $y = 0$ and $z = 0$ planes. The burning was initiated at the center of WD by filling a small spherical region at $r < 0.015R_{WD}$ with hot reaction products without disturbing the hydrostatic equilibrium.

The development of the explosion for the high-resolution case is shown in Fig. 1 by a series of 3D snapshots of the flame and WD surfaces (see also Movies S1 and S2). At the beginning, the initially spherical flame ignited in the center of WD propagates outwards with the normal laminar flame speed S_l . As it moves away from the center, the gravitational acceleration g and the Atwood number A increase. This increases the amplitude and rate of development of the RT instability controlled by g and A . Due to the RT instability, small perturbations of the flame surface grow and form a few plumes that have characteristic mushroom shapes. The turbulent flame speed S_t also increases with g and A according to Eq.(2), and eventually dominates S_l in Eq.(1). The flame plumes continue to grow, due partially to the flame propagation and partially to gravitational forces that cause the hot, burnt, low-density material inside the plumes to rise towards the WD surface. The same gravitational forces also pull the cold, high-density unburnt material between the plumes down towards the center. The resulting shear flows along the flame surface are unstable (Kelvin-Helmholtz (KH) instability) and quickly develop vortices. These vortices further distort the flame surface, and also contribute their energy into the turbulent cascade that creates turbulent motions at smaller scales, down to a few dx .

When the original flame plumes grow large enough, secondary RT instabilities develop on their surface, thus producing the next level of “mushrooms” that also grow and may become subject to the RT instability at a smaller scale, etc. These smaller gravity-induced mushrooms interact with the turbulence created by the previous generation of larger flame plumes, and also produce some turbulence themselves through the KH instability. The resulting complicated turbulent flame surface is shown in Fig. 1.

As the turbulent flame develops, the energy released by the thermonuclear burning causes the WD to expand. The expansion accelerates and becomes nonuniform as the rising plumes approach the star surface. We continued the simulations until the star surface reached the computational domain boundary. By that time, the radius of the expanding star increased by about a factor of 2.6, the outer layers accelerated to about 1.2×10^9 cm/s, and the density of unburnt material near the star center decreased to about 5×10^7 g/cm³. The area around the center still contains a significant amount of unburnt material that sinks at 10^8 cm/s towards the center between large flame plumes. The velocity of the large flame plumes is essentially zero relative to the expanding matter, that is, the plumes have practically stopped rising. This effect of freezing of the RT-instability on large scales due to expansion is also related to freezing of large-scale turbulence (37), and contributes to the burning-rate decrease after 1.5 s.

Effects of initial composition and background turbulence. Before we compare the computed supernova explosion with astronomical observations, we need to know the extent to which the results are affected by uncertainties in initial model parameters. We examined two properties of the WD that are not well defined and are expected to have the most pronounced effect on the explosion, the initial composition and the level of background turbulence.

In the base case described above, we assumed a uniform composition with the carbon mass fraction $X_C = 0.5$. A WD can also have a core partially depleted of carbon (42). To take this into account, we calculated the explosion for $X_C = 0.25$ in the core and $X_C = 0.5$ in the outer layers. The core with the radius $0.25R_{WD}$ contained about 25% of the total mass of the WD. The lower C concentration resulted in a slightly slower explosion as shown in Fig. 2 by the total energy E_{tot} , the kinetic energy E_k , the released nuclear energy E_n , and the burnt mass fraction f_b as functions of time. Compared to the base case, it takes about 0.2 seconds longer for the slower explosion to release the same amount of energy. There is no significant difference in the turbulent flame structure.

The background turbulence is created by intense convective flows that appear when the accreting WD approaches the Chandrasekhar limit and quickly contracts just before ignition. A flame propagating through intense turbulent flow can be accelerated to the velocity of turbulent motions, V_t . Two-dimensional simulations (42) show that V_t estimated as a differential velocity between adjoining eddies with sizes $\sim 10^7$ cm can reach 2.4×10^7 cm/s in central parts of a WD. To model this effect, we replaced Eq.(1) by

$$S = \max(S_l, S_t, V_t) \quad (3)$$

and assumed that V_t has a constant value V_t^0 for $r < 0.33R_{WD}$, and linearly decreases to 0 as r approaches R_{WD} . The simulations were performed for $V_t^0 = 3 \times 10^7$ cm/s. The results (Fig. 2) show that the background turbulence significantly increases the energy-release rate and the expansion at the initial stage of the explosion. During the first 0.45 s, the explosion with the background turbulence releases the same amount of energy as the base case during 0.8 s. The material burns faster because the laminar flame speed ($\sim 10^7$ cm/s), which played an important role at the initial stage for the base case, was replaced by a higher value of V_t according to Eq.(3). The initial flame speed, however, also has a long-lasting effect because the initial stage of explosion is critical for the development of the turbulent flame surface. A flame that initially propagates with a higher speed competes with the RT instability more efficiently and develops fewer wrinkles on resolved scales. This results in a smaller surface area of the flame. As the flame propagates outwards, S_t increases for both cases. It becomes higher than S_l for the base case, and higher than V_t for the case with the background turbulence. S_t is approximately the same for both cases, but the explosion with the background turbulence begins to slow down when the burnt mass fraction f_b reaches 0.15 because of a smaller flame surface area, and eventually releases much less energy than the base case.

If we increase V_t^0 to the unrealistically high value 10^8 cm/s, the background turbulence dominates even far from the center and the RT instability does not develop at all. The flame surface is almost spherical until the end of the simulation, and there is no unburnt material below the flame surface. The energy release and expansion are fast (Fig. 2) until the flame reaches low-density layers where the C burning almost stops. The final values of E_{tot} , E_k , E_n , and f_b are higher than for $V_t^0 = 3 \times 10^7$ cm/s, but lower than for the base case in which the highly convoluted turbulent flame continues to burn high-density material in central parts of the WD.

The uncertainty in the maximum energy released by the explosion can be estimated as the difference between the base case and the case with $V_t^0 = 3 \times 10^7$ cm/s (Fig. 2). Even though the burning continues for the base case, it begins to slow down and will stop when the density of the unburnt material near the center drops below $\simeq 10^6$ g/cm³. We expect that by that time, the burnt mass fraction will increase to 0.6-0.7, which is 1.7-2 times higher than for the case with the background turbulence. The final released energies for these two cases will also differ by a factor of 1.7-2 ($E_n \simeq 0.87 \times 10^{51}$ ergs for $V_t^0 = 3 \times 10^7$ cm/s, and $E_n \simeq (1.5 - 1.7) \times 10^{51}$ ergs for the base case).

Comparison of simulations and observations. Now, after ensuring numerical convergence and examining the sensitivity to initial conditions, we can try to compare results of simulations to astronomical observations. One important parameter that can be directly compared to observations is the kinetic energy of the expanding material. This energy can be calculated from expansion velocities measured using

the Doppler shift of spectral lines. The typical kinetic energy for SN Ia is $(1 - 1.5) \times 10^{51}$ ergs (6). In simulations, this energy corresponds to E_k at infinity, when all the nuclear energy released transforms into kinetic energy of the expanding material and the work against gravity: $E_k = E_n + E_{tot}^0$. The negative initial value $E_{tot}^0 = -0.5 \times 10^{51}$ represents the binding energy of the star. For our base case, the estimated final value $E_k = E_n - 0.5 \times 10^{51} \simeq (1.0 - 1.2) \times 10^{51}$ ergs is at the lower end of the typical range. The case with the realistic level of background turbulence, $V_t^0 = 3 \times 10^7$ cm/s, produces a weak explosion, with final $E_k \simeq 0.37 \times 10^{51}$ ergs. The explosion is also not strong enough ($E_k = 0.6 \times 10^{51}$ ergs) for the high level of background turbulence, $V_t^0 = 10^8$ cm/s. For all the cases shown in Fig. 2, the final value of E_{tot} is positive, that is, the explosion releases enough energy to unbind the star. The base-case 3D explosion is much more energetic than explosions resulted from two-dimensional simulations (43,26,34) because the flame does not develop enough surface area in two dimensions as discussed in (44).

The key feature of the simulations is the highly convoluted turbulent flame surface that allows extensive interpenetration of burnt and unburnt materials. The angle-averaged burnt mass fraction at 1.9 s is less than 1 for any distance r from the WD center (Fig. 3). In particular, 80 – 90% of the material near the WD center is unburnt. This material continues to burn, but it will not burn out completely as long as convective flows supply fresh unburnt material from outer layers. As the WD continues to expand, the density decreases. The deflagration begins to produce intermediate-mass elements when the density of unburnt material becomes lower than $\simeq 5 \times 10^7$ g/cm³, and the burning stops when the density drops below $\simeq 10^6$ g/cm³. This means that the final ejecta produced by the 3D deflagration model will contain the unburnt material and intermediate-mass elements at any distance from the center.

The unburnt carbon and oxygen that remain between the flame plumes and intermediate-mass elements that form at low densities at different r should produce spectral signatures in a wide range of expansion velocities, including low velocities close to zero. Analyses of SN Ia spectra, however, imply C (45-47) and O (48) only at high velocities, as would be produced by the acceleration of expanding outer layers. For intermediate-mass elements, minimum observed velocities are lower (2), but large enough ($\sim 10,000$ km/s for Si) to rule out the presence of these elements near the WD center. In the simulations, the low-velocity unburnt material was not present only for the case with an unrealistically high level of background turbulence that produced a spherical flame and resulted in a weak explosion.

The dynamics of the 3D deflagration described here is in agreement with the preliminary simulations (33) performed with the same model. These results were independently confirmed by Reinecke et al. (34,35) who used different subgrid model, nuclear kinetics scheme and initial conditions, and obtained similar highly convoluted flames with unburnt material near the WD center.

We thus conclude that the deflagration model of a SN Ia explosion is incomplete. The most natural solution to this problem that would make the results consistent with observations would be to assume that the turbulent flame triggers a detonation. A thermonuclear detonation wave could propagate through the WD with velocities $\sim 10^9$ cm/s (49,50) and would quickly burn all the material near the center leaving only the low-density outer layers unburnt. For the density below 5×10^7 g/cm³, a detonation would produce intermediate-mass elements (25) that are observed in spectra of SNe Ia. A detonation would also partially smooth out composition inhomogeneities that are predicted by the deflagration model and may be incompatible with observations (51). Remaining asymmetries may account for a weak polarization recently detected in SN Ia spectra (52,53).

One-dimensional (25,28-32) and two-dimensional (26,27) delayed-detonation models were the most successful in explaining observable characteristics of SNe Ia. These models, however, use the time for detonation initiation as a free parameter because the DDT problem is intrinsically 3D and still unsolved. A large-scale 3D model also cannot reproduce DDT phenomena that involve physical processes occurring on small unresolved scales. One approach to solving this problem is to study, in much more detail, the types of reacting flows created by 3D deflagrations and look for situations that create the right types of “hot spots” that we know (54) are the sources of detonation initiation.

References and Notes

1. J. C. Wheeler, R. P. Harkness, *Rep. Prog. Phys.* **53**, 1467 (1990).
2. A. V. Filippenko, *Annu. Rev. Astron. Astrophys.* **35**, 309 (1997)
3. J. C. Wheeler, *Am. J. Phys.*, in press (2002)
4. S. E. Woosley, T. A. Weaver, *Annu. Rev. Astron. Astrophys.* **24**, 205 (1986)
5. D. Branch, A. M. Khokhlov, *Phys. Rep.* **256**, 53 (1995)
6. J. C. Wheeler, R. P. Harkness, A. M. Khokhlov, P. A. Höflich, *Phys. Rep.* **256**, 211 (1995)
7. K. Nomoto, K. Iwamoto, N. Kishimoto, *Science* **276**, 1378 (1997)
8. D. Branch, *Annu. Rev. Astron. Astrophys.* **36**, 17 (1998)
9. W. Hillebrandt, J. C. Niemeyer, *Annu. Rev. Astron. Astrophys.* **38**, 191 (2000)
10. A. Burrows, *Nature* **403**, 727 (2000)
11. F. Hoyle, W. A. Fowler, *Astrophys. J.* **132**, 565 (1960).
12. M. M. Phillips, *Astrophys. J.* **413**, L105 (1993)
13. M. Hamuy *et al.*, *Astron. J.* **109**, 1 (1995)
14. A. G. Riess, W. H. Press, R. P. Kirshner, *Astrophys. J.* **438**, L17 (1995)
15. S. Perlmutter *et al.*, *Nature* **391**, 51 (1998)
16. S. Perlmutter *et al.*, *Astrophys. J.* **517**, 565 (1999)
17. B. P. Schmidt *et al.*, *Astrophys. J.* **507**, 46 (1998)
18. A. G. Riess *et al.*, *Astron. J.* **116**, 1009 (1998)
19. A. G. Riess *et al.*, *Astrophys. J.* **560**, 49 (2001)
20. P. A. Höflich *et al.*, *Astrophys. J.* **472**, L81 (1996)
21. W. D. Arnett, *Astrophys. Space Sci.* **5**, 180 (1969)
22. C. J. Hansen, J. C. Wheeler, *Astrophys. Space Sci.* **3**, 464 (1969)
23. K. Nomoto, D. Sugimoto, S. Neo, *Astrophys. Space Sci.* **39**, L37 (1976)
24. K. Nomoto, F.-K. Thielemann, K. Yokoi, *Astrophys. J.* **286**, 644 (1984)
25. A. M. Khokhlov, *Astron. Astrophys.* **245**, 114 (1991)
26. D. Arnett, E. Livne, *Astrophys. J.* **427**, 315 (1994)
27. D. Arnett, E. Livne, *Astrophys. J.* **427**, 330 (1994)
28. H. Yamaoka, K. Nomoto, T. Shigeeyama, F.-K. Thielemann, *Astrophys. J.* **393**, L55 (1992)
29. A. M. Khokhlov, E. Müller, P. A. Höflich, *Astron. Astrophys.* **270**, 223 (1993)
30. P. A. Höflich, *Astrophys. J.* **443**, 89 (1995)
31. P. A. Höflich, A. M. Khokhlov, J. C. Wheeler, *Astrophys. J.* **444**, 831 (1995)
32. P. A. Höflich, A. M. Khokhlov, *Astrophys. J.* **457**, 500 (1996)
33. A. M. Khokhlov, <http://www.arxiv.org/abs/astro-ph/0008463> (2000)
34. M. Reinecke, W. Hillebrandt, J. C. Niemeyer, *Astron. Astrophys.* **386**, 936 (2002)
35. M. Reinecke, W. Hillebrandt, J. C. Niemeyer, *Astron. Astrophys.*, **391**, 1167 (2002)
36. Materials and methods are available as supporting material on Science Online.
37. A. M. Khokhlov, *Astrophys. J.* **449**, 695 (1995)
38. A. M. Khokhlov, *J. Comput. Phys.* **143**, 519 (1998)
39. F. X. Timmes, S. E. Woosley, *Astrophys. J.* **396**, 649 (1992)
40. A. M. Khokhlov, E. S. Oran, J. C. Wheeler, *Astrophys. J.* **478**, 678 (1997)
41. A. M. Khokhlov, E. S. Oran, J. C. Wheeler, *Combust. Flame* **105**, 28 (1996)
42. P. A. Höflich, J. Stein, *Astrophys. J.* **568**, 779 (2002)
43. E. Livne, *Astrophys. J.* **406**, L17 (1993)
44. A. M. Khokhlov, *Astrophys. J.* **424**, L115 (1994)
45. D. J. Jeffery *et al.*, *Astrophys. J.* **397**, 304 (1992)
46. A. Fisher, D. Branch, P. Nugent, E. Baron, *Astrophys. J.* **481**, L89 (1997)
47. P. A. Mazzali, *Mon. Not. R. Astron. Soc.* **321**, 341 (2001)
48. R. P. Kirshner *et al.*, *Astrophys. J.* **415**, 589 (1993)
49. A. M. Khokhlov, *Mon. Not. R. Astron. Soc.* **239**, 785 (1989)
50. V. N. Gamezo, J. C. Wheeler, A. M. Khokhlov, E. S. Oran, *Astrophys. J.* **512**, 827 (1999)
51. R. C. Thomas, D. Kasen, D. Branch, E. Baron, *Astrophys. J.* **567**, 1037 (2002)

52. L. Wang, J. C. Wheeler, P. A. Höflich, *Astrophys. J.* **476**, L27 (1997)
53. D. A. Howell, P. A. Höflich, L. Wang, J. C. Wheeler, *Astrophys. J.* **556**, 302 (2001)
54. A. M. Khokhlov, E. S. Oran, *Combust. Flame* **119**, 400 (1999)
55. This work was supported in part by the NASA ATP program (NRA-99-01-ATP-130) and by the Naval Research Laboratory (NRL) through the Office of Naval Research. Computing facilities were provided by the DOD HPCMP program. We would like to thank David Branch, Peter Höflich, Eli Livne, Martin Reinecke, Lifan Wang, and Craig Wheeler for helpful discussions, and the referees for useful comments.

Supporting Online Material

www.sciencemag.org

Materials and Methods

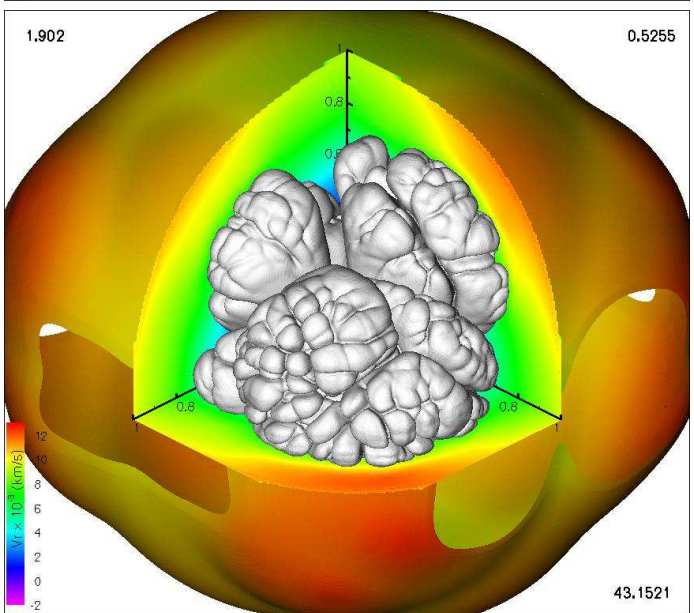
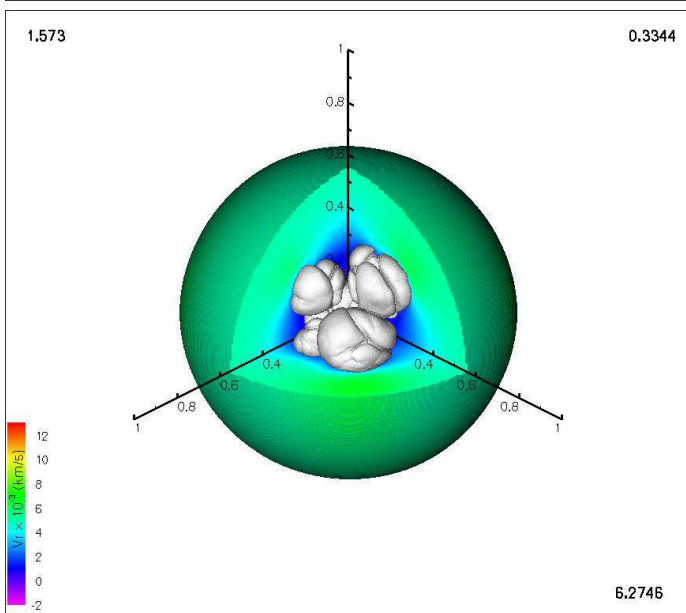
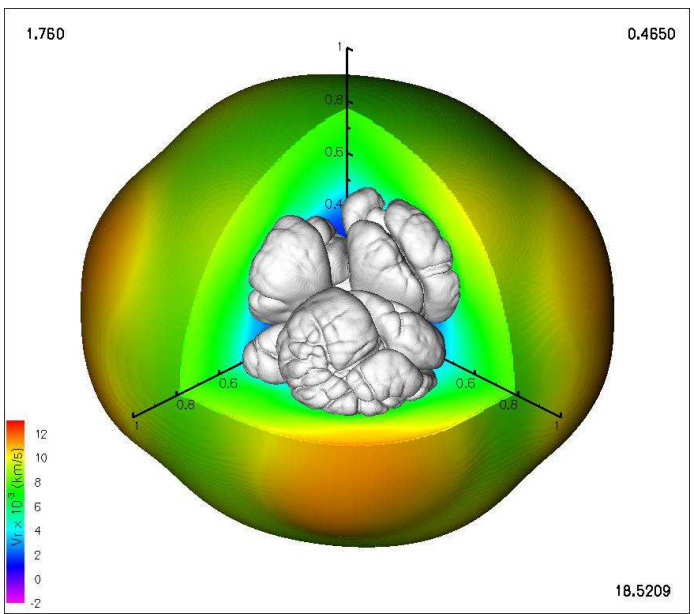
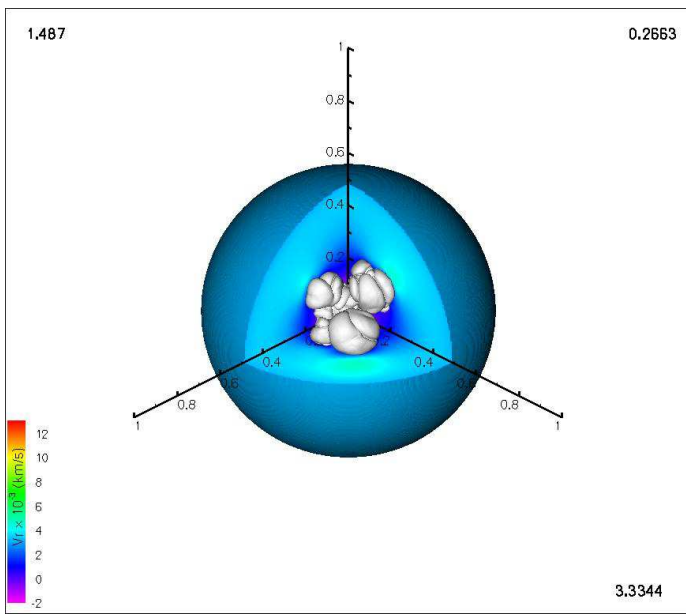
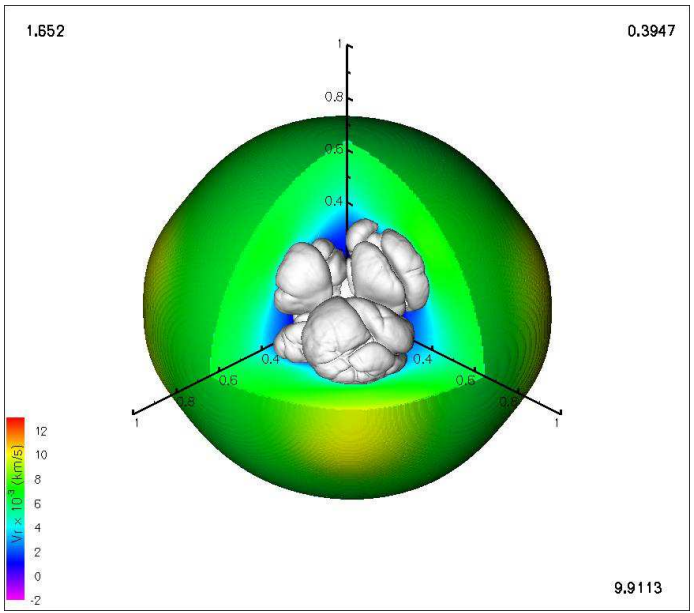
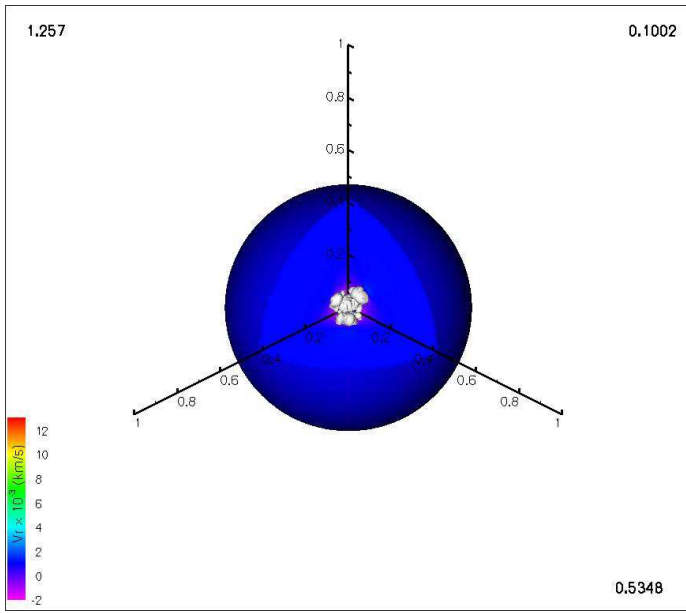
Figs. S1, S2

Table S1

Movies S1, S2

FIGURES

Fig. 1. Development of thermonuclear deflagration in carbon-oxygen white dwarf. The gray surface shows the turbulent thermonuclear flame. The color scale shows the radial velocity of unburnt material scaled by 1000 km/s. Distances are scaled by the computational domain size $x_{max} = 5.35 \times 10^8$ cm. Numbers in the frame corners are time in seconds (left top), burnt mass fraction f_b (right top), and flame surface area scaled by x_{max}^2 (right bottom). High resolution ($dx_{min} = 2.6 \times 10^5$ cm). $L = 2dx$.



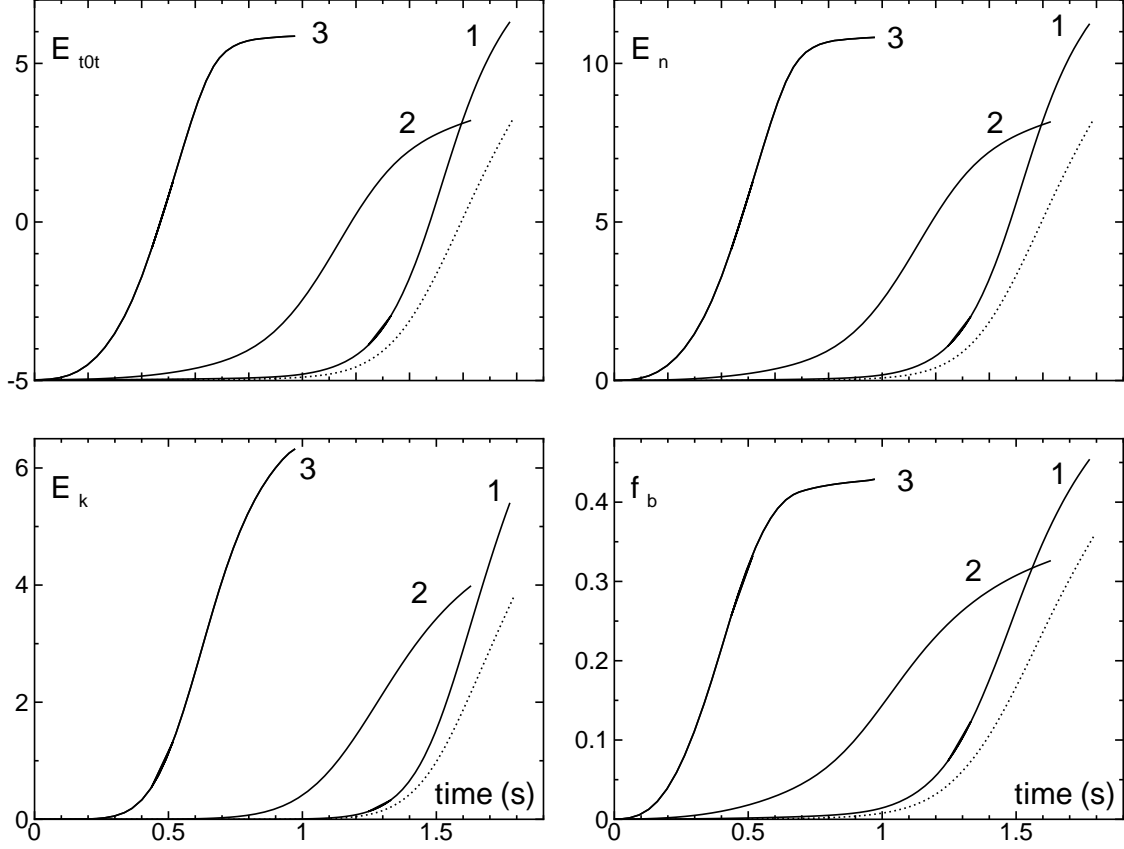


Fig. 2. Total ($E_{tot} = E_k + E_t - E_g$), kinetic (E_k), released nuclear (E_n) energies and the burnt mass fraction f_b as functions of time for the base case without background turbulence (1), with background turbulence $V_t^0 = 3 \times 10^7$ cm/s (2), and $V_t^0 = 10^8$ cm/s (3). Dotted lines correspond to reduced carbon concentration $X_C = 0.25$ in the core. Energy units are 10^{50} ergs. Medium resolution ($dx_{min} = 5.2 \times 10^5$ cm). $L = dx$.

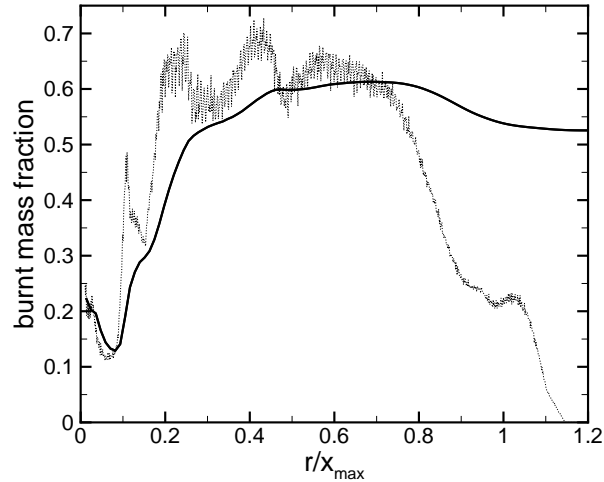


Fig. 3. Angle-averaged local mass fraction of burnt material (dotted line) and total burnt mass fraction inside a spherical region of radius r (solid line) as functions of distance r from the WD center. The distance is scaled by the computational domain size $x_{max} = 5.35 \times 10^8$ cm. Time 1.9 s corresponds to the last frame of Fig. 1.

Supporting Online Material

V. N. Gamezo, A. M. Khokhlov, E. S. Oran, A. Y. Chtchelkanova, R. O. Rosenberg. Explosions of Thermonuclear Supernovae: Physical Implications of Full-Scale, Three-Dimensional Simulations.

MATERIALS AND METHODS

NRL Supernova Model

Fluid Dynamics and Equation of State

The numerical model is based on reactive Euler equations

$$\begin{aligned}\frac{\partial \rho}{\partial t} &= -\nabla \cdot (\rho \mathbf{U}) , \\ \frac{\partial \rho \mathbf{U}}{\partial t} &= -\nabla \cdot (\rho \mathbf{U} \mathbf{U}) - \nabla P + \rho \mathbf{g} , \\ \frac{\partial E}{\partial t} &= -\nabla \cdot (\mathbf{U} (E + P)) + \rho \mathbf{U} \cdot \mathbf{g} + \rho \dot{q} ,\end{aligned}$$

where ρ , $E = E_i + \rho U^2/2$, E_i , \mathbf{U} , \mathbf{g} and \dot{q} are the mass density, energy density, internal energy density, velocity of matter, gravitational acceleration, and nuclear energy release rate per unit mass, respectively. These equations describe mass, momentum, and energy conservation laws for an inviscid fluid. The thermodynamic properties of the fluid are defined by the equation of state of degenerate matter, which is well described by basic theory and includes contributions from ideal Fermi-Dirac electrons and positrons, equilibrium Planck radiation, and ideal ions. Pressure $P = P(\rho, E_i, Y_e, Y_i)$ and temperature $T = T(\rho, E_i, Y_e, Y_i)$ are determined by the equation of state as functions of ρ , E_i , the electron mole fraction Y_e , and the mean mole fraction of ions Y_i . The relation between P and ρ is close to that in a polytropic gas with γ varying from 4/3 to 5/3. This equation of state is valid for the thermodynamic parameters and compositions expected in the computations, ranging from relatively cold highly degenerate carbon-oxygen matter to partially degenerate hot products of thermonuclear reactions.

Nuclear Kinetics and Flame Propagation

Thermonuclear reactions involved in the thermonuclear burning of the carbon-oxygen mixture (*S1-S3*) can be separated into three consecutive stages responsible for the energy release. First, the $^{12}\text{C} + ^{12}\text{C}$ reaction leads to the consumption of C and formation of mostly Ne, Mg, protons, and α -particles. Then begins the nuclear statistical quasi-equilibrium (NSQE) stage, during which O burns out and Si-group (intermediate mass) elements are formed. Finally, Si-group elements are converted into the Fe-group elements and the nuclear statistical equilibrium (NSE) sets in. The reaction time scales associated with these stages strongly depend on temperature and density and may differ from one another by several orders of magnitude (*S4-S8*).

The full nuclear reaction network includes hundreds of species that participate in thousands of reactions. Integration of this full network is too time-consuming to be used in multidimensional numerical models. Therefore, we used a simplified four-equation kinetic scheme (*S9,S10*) that describes all major stages of carbon burning. This kinetic scheme is coupled with a flame-capturing algorithm (*S11,S10*) that ensures thermonuclear flame propagation with a prescribed speed S . Flame capturing is needed because we cannot resolve in large-scale simulations the physical thickness of a laminar flame that differs from the white dwarf radius R_{WD} by up to 12 orders of magnitude.

Numerical Method

The fluid dynamic equations, coupled to the nuclear reaction mechanism and the flame-capturing algorithm are integrated using an explicit, second-order, Godunov-type, adaptive-mesh-refinement code (*S11,S12*). A Riemann solver is used to evaluate fluxes at cell interfaces. The computational mesh is

comprised of cubic cells of various sizes that are organized in a fully threaded tree (FTT) (S12). The FTT-based parallel adaptive mesh refinement algorithm dynamically adjusts cell sizes in accordance with changing physical conditions in the vicinity of each cell. Here, the mesh was refined around shock waves, flame fronts, and in regions of steep gradients of density, pressure, composition, and tangential velocity. The cell size dx varies within predefined limits dx_{min} and dx_{max} in such a way that neighboring cell sizes can be the same or differ by a factor of two. The code has been extensively tested and used in various combustion problems involving shocks, flames, turbulence, and their interactions (S13,S14, and references therein) and in astrophysics (S15).

Initial Conditions

The initial conditions for the simulations were set up for a Chandrasekhar-mass white dwarf (WD) in hydrostatic equilibrium with the initial radius $R_{WD} = 2 \times 10^8 cm$, the initial central density $\rho_c = 2 \times 10^9 g/cm^3$, the uniform initial temperature $T = 10^5 K$, and the uniform initial composition with equal mass fractions of ^{12}C and ^{16}O nuclei. Starting from the central pressure $P(\rho_c)$, the equations of hydrostatic equilibrium, $dP/dr = -GM\rho/r^2$ and $dM/dr = 4\pi\rho r^2$, were integrated outward until $P = 0$ was reached (here G is the gravitational constant, and M is the mass of the material inside a sphere of radius r). The resulting WD configuration was interpolated onto a 3D mesh extended from the WD center $x = y = z = 0$ to $x = y = z = 2.6R_{WD}$. Thus, we model one octant of the WD assuming mirror symmetry along the $x = 0$, $y = 0$ and $z = 0$ planes. The burning was initiated at the center of WD by filling a small spherical region at $r < 0.015R_{WD}$ with hot reaction products without disturbing the hydrostatic equilibrium.

Because a Chandrasekhar-mass WD is close to a collapse threshold, its gravitational equilibrium is sensitive to the discretization errors that appear when the spherical body is mapped into a Cartesian mesh. To minimize these errors, the mesh is initially refined to the finest level near the WD center ($r < 0.4R_{WD}$). During the simulations, we keep the mesh unchanged until the flame reaches the fine grid boundary. Then the adaptive mesh refinement algorithm is turned on.

Subgrid Model for Flame Speed

The speed of a laminar thermonuclear flame in a WD is defined by reaction rates and transport properties of the material and governed by the same laws that describe laminar flame structure in terrestrial chemical systems (S16-S18). The only substantial difference is that transport properties of degenerate matter are dominated by the electron heat conduction at high densities, and by both electron and photon heat conduction at low densities. The steady-state laminar flame speed S_l in carbon-oxygen degenerate matter is a known function of temperature, density, and composition (S19,S20), but the flame can be laminar only near the center of a WD. Away from the center, the flame is turbulent and propagates with a higher effective speed (S21,S11,S22,S23).

In our simulations, the turbulent flame speed S_t is defined by a subgrid model that takes into account physical processes at scales smaller than the computational cell size. The subgrid model assumes that burning on small unresolved scales is driven by the gravity-induced Rayleigh-Taylor (RT) instability. This instability distorts the flame surface at multiple scales and generates turbulent motions in the surrounding fluid. The turbulent energy propagates from large to small scales, thus further disturbing the flame surface on small scales. A developed turbulent flame is statistically steady-state and forms a dynamic hierarchical self-similar 3D structure where the flame surface is distorted at multiple scales. The flame distortions increase the flame surface and, therefore, the burning rate. The larger the scale, the higher the burning rate at this scale due to the increase of the flame surface resulting from distortions at smaller scales. The burning rate defines the turbulent flame speed S_t for any given length scale. This turbulent flame structure was analyzed in 3D numerical simulations (S11,S24) performed for the thermonuclear burning of carbon-oxygen degenerate matter in a uniform gravitational field. It was found that a turbulent flame in a vertical column of width L becomes quasi-steady-state and propagates with the speed

$$S_t \simeq 0.5\sqrt{AgL} \tag{S1}$$

independent of the laminar speed S_l , where $A = (\rho_0 - \rho_1)/(\rho_0 + \rho_1)$ is the Atwood number, and ρ_0 and ρ_1 are the densities ahead and behind the flame front, respectively. We used this result in the subgrid

model assuming that at $L \ll R_{WD}$ burning can be considered as locally steady state (S25,S26,S11). The driving scale L was set equal to the computational cell size dx . The resulting flame velocity S used by the flame-capturing algorithm was calculated as

$$S = \max(S_l, S_t) \tag{S2}$$

Numerical Convergence

Numerical convergence tests, which are critical for establishing the validity of any numerical simulations, are performed to ensure that the solution obtained is not significantly affected by the computational cell size dx . In our case, numerical convergence is closely related to the physics of the subgrid model that defines the turbulent flame speed in Eq.(S1) and assumes that burning can be considered as locally steady state. The steady-state assumption is not valid for length scales affected by the spherical geometry and expansion. These scales need to be explicitly resolved, but this will not necessarily ensure that the solution is independent of dx . The resolved flame properties should also correspond to the flame properties built into the subgrid model.

The subgrid model is based on the two main properties of a turbulent flame (S11,S24): self-similarity of the flame structure and self-regulation of the flame speed. Self-similarity means that the 3D distortions of the flame surface at different scales are similar. Self-regulation means that changing the flame speed at small scales does not affect the flame speed at larger scales. This occurs because a higher flame speed at small scales causes small flame wrinkles to burn out, thus decreasing the flame surface. The resulting burning rate, defined as a product of the flame speed at small scales and the flame surface, does not change. This subgrid model makes it possible to reproduce the correct flame propagation in numerical simulations while explicitly resolving only the large-scale flame structure. If the resolved flame structure is self-similar and self-regulating, and behaves according to the Eq.(S1), the subgrid model just extends this behavior to unresolved small scales. Shifting the boundary between resolved and unresolved scales by changing the numerical resolution should not affect the turbulent flame propagation. The solution obtained should then be independent of numerical resolution and on the exact value of S_t .

We performed a series of computations with three resolutions: low ($dx_{min} = 10.5 \times 10^5$ cm), medium ($dx_{min} = 5.2 \times 10^5$ cm), and high ($dx_{min} = 2.6 \times 10^5$ cm). The maximum computational cell size $dx_{max} = 41.8 \times 10^5$ cm and the computational domain size $x_{max} = 5.35 \times 10^8$ cm were kept constant. The development of the explosion for the high-resolution case is shown in Fig. 1 and described in the main text. The simulation with medium resolution showed a similar pattern of development, though it produced fewer small-scale wrinkles on the flame surface. The low-resolution simulation showed only the largest flame plumes. The surface of these plumes remained smooth and did not develop any significant instabilities. These three cases are compared in Fig. S1, which shows the total energy E_{tot} , the kinetic energy E_k , the released nuclear energy E_n , and the burnt mass fraction f_b as functions of time for the developing explosions. The curves for high and medium resolutions practically coincide for E_{tot} , E_n , and f_b . The kinetic energy E_k shows the largest difference between the high-resolution and the medium-resolution cases, and this does not exceed 10%. Therefore, the solution is practically converged.

In order to test the self-regulating properties of the flame, we increased L in Eq.(S1) by a factor of 2 ($L = 2dx$), and repeated the three simulations with the same high, medium, and low numerical resolutions. The key energies and f_b for these simulations are compared with previous three cases in Fig. S2. For the low-resolution case, the self-regulation mechanism on resolved scales does not work, S_t and key energies increase by the same factor $\sqrt{2}$. For the medium and high resolutions, the self-regulation appears on resolved scales and reduces the maximum difference between the energies calculated for different S_t to 15% and 6%, respectively. These tests show that the numerical convergence was achieved in the high- and medium-resolution simulations. The 3D structure of the turbulent flame was resolved in sufficient detail to reproduce key dynamic properties of the flame included in the subgrid model. The results are self-consistent and reasonably accurate, and can be used to analyze explosion scenarios for thermonuclear supernovae.

SUPPORTING FIGURES

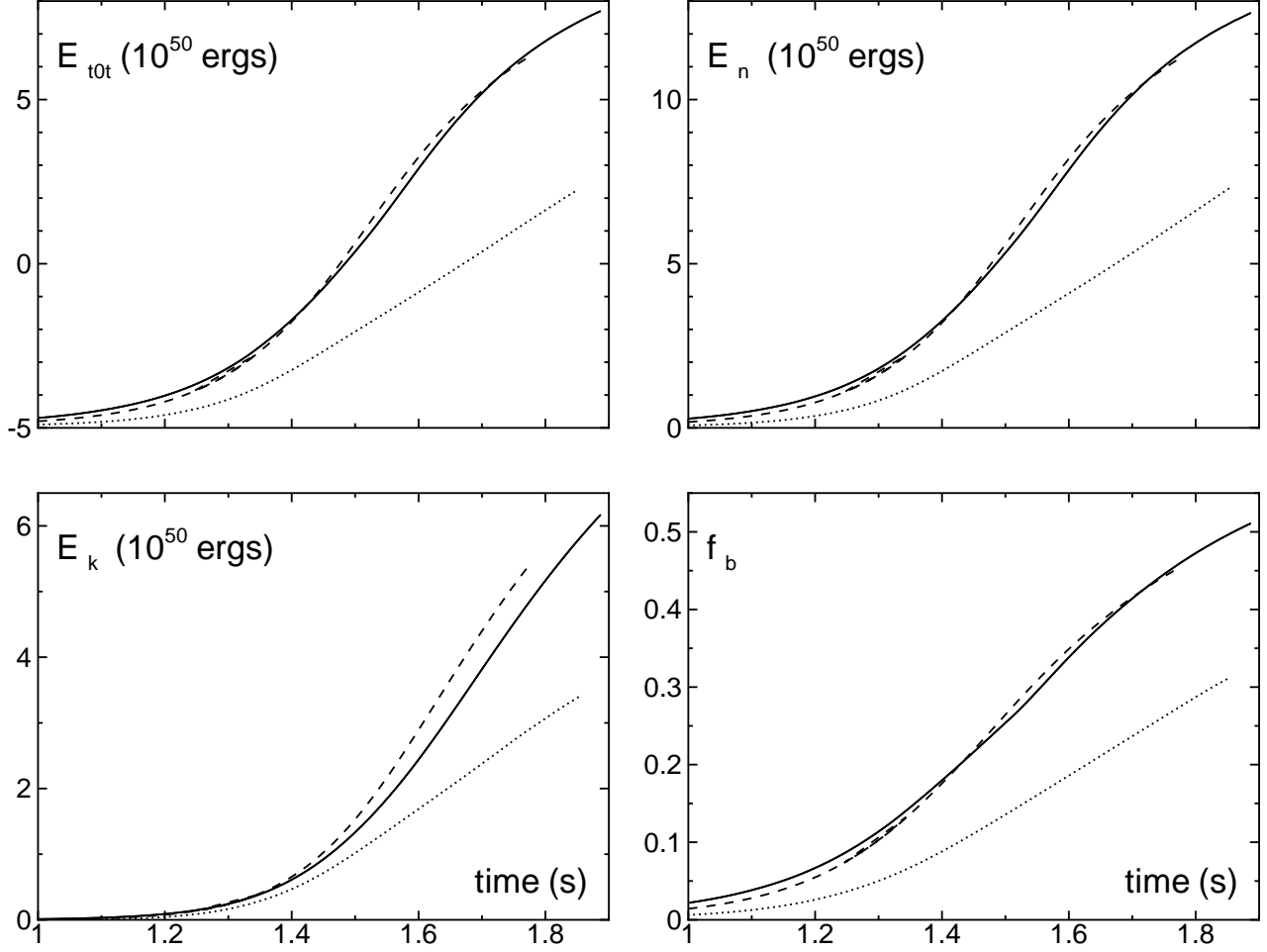


Fig. S1. Total (E_{tot}), kinetic (E_k), released nuclear (E_n) energies and the burnt mass fraction f_b as functions of time. Solid, dashed, and dotted lines correspond to high, medium, and low numerical resolution, respectively. E_k is calculated from local fluid velocities and densities as a total for all computational cells. The conservation law $E_k + E_t - E_n - E_g = const$ is satisfied with accuracy better than 1%.

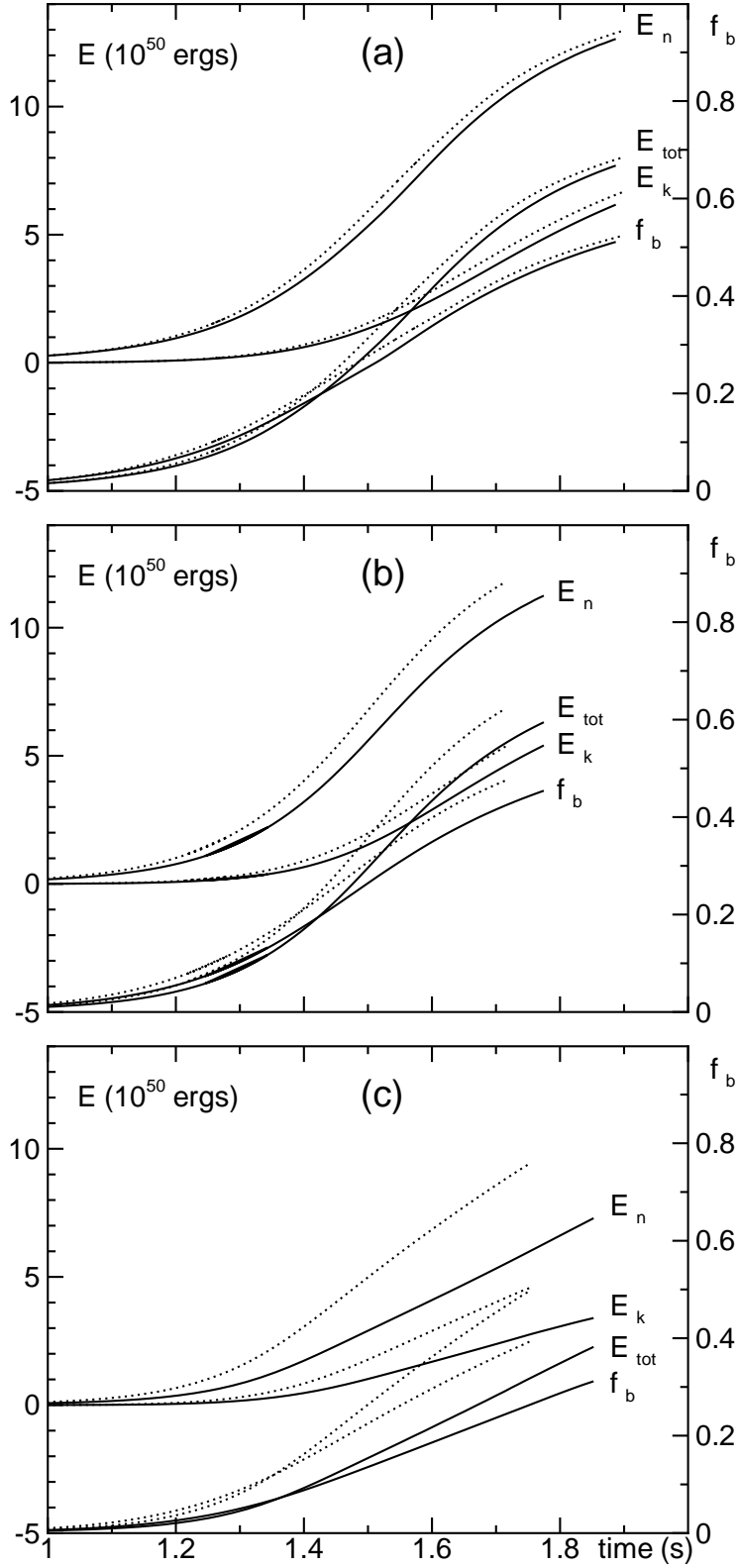


Fig. S2. Total (E_{tot}), kinetic (E_k), released nuclear (E_n) energies and the burnt mass fraction f_b as functions of time for high (a), medium (b) and low (c) numerical resolutions, $L = dx$ (solid lines) and $L = 2dx$ (dotted lines).

SUPPORTING TABLES

Table S1. Parameters displayed in Movie 2.

Parameters	Definition	
<i>step,</i>	<i>fburn</i>	timestep, mass fraction of burnt material
<i>time,</i>	<i>rhomax</i>	time (s), maximum mass density in computational domain (g/cm ³)
<i>fsurf,</i>	<i>fsurf1</i>	flame surface area ⁽¹⁾ , $fsurf1 = fsurf / (4\pi r_{fmax}^2)$
<i>rfmin,</i>	<i>rfmax</i>	min, max distance from star center to flame surface ⁽²⁾
<i>ssurf,</i>	<i>ssurf1</i>	star surface area ⁽¹⁾ , $ssurf1 = ssurf / (4\pi r_{smax}^2)$
<i>rsmmin,</i>	<i>rsmmax</i>	min, max distance from star center to star surface ⁽²⁾
<i>vrsmmin,</i>	<i>vrsmmax</i>	min, max radial flow velocity at star surface (cm/s)
<i>vrmin,</i>	<i>vrmax</i>	min, max radial flow velocity in computational domain (cm/s)
<i>etherm</i>		thermal energy ⁽³⁾
<i>ekin</i>		kinetic energy ⁽³⁾
<i>egrav</i>		gravitational energy ⁽³⁾
<i>etot</i>		total energy = etherm + ekin - egrav ⁽³⁾
<i>enuc</i>		nuclear energy ⁽³⁾

⁽¹⁾ scaled by x_{max}^2

⁽²⁾ scaled by $x_{max} = 5.35 \times 10^8$ cm.

⁽³⁾ scaled by 10^{50} ergs

SUPPORTING REFERENCES AND NOTES

- S1. W. A. Fowler, G. R. Caughlan, B. A. Zimmerman, *Annu. Rev. Astron. Astrophys.* **13**, 69 (1975)
- S2. S. E. Woosley, W. A. Fowler, J. A. Holmes, B. A. Zimmerman, *Atomic Data and Nuclear Data Tables*, **22**, 371 (1978)
- S3. F.-K. Thielemann, M. Arnould, J. W. Truran, in *Advances in Nuclear Astrophysics*, E. Vangioni-Flam, Ed. (Editions frontières, Gif-sur-Yvette, 1987), p.525
- S4. J. W. Truran, A. G. W. Cameron, A. Gilbert, *Canadian J. of Phys.* **44**, 563 (1966)
- S5. D. Bodansky, D. D. Clayton, W. A. Fowler, *Astrophys. J. Suppl. Ser.* **16**, 299 (1968)
- S6. S. E. Woosley, W. D. Arnett, D. D. Clayton, *Astrophys. J. Suppl. Ser.* **26**, 231 (1973)
- S7. A. M. Khokhlov, *Mon. Not. R. Astron. Soc.* **239**, 785 (1989)
- S8. V. N. Gamezo, J. C. Wheeler, A. M. Khokhlov, E. S. Oran, *Astrophys. J.* **512**, 827 (1999)
- S9. A. M. Khokhlov, *Astron. Astrophys.* **245**, 114 (1991)
- S10. A. M. Khokhlov, <http://www.arxiv.org/abs/astro-ph/0008463> (2000)
- S11. A. M. Khokhlov, *Astrophys. J.* **449**, 695 (1995)
- S12. A. M. Khokhlov, *J. Comput. Phys.* **143**, 519 (1998)
- S13. A. M. Khokhlov, E. S. Oran, *Combust. Flame* **119**, 400 (1999)
- S14. V. N. Gamezo, A. M. Khokhlov, E. S. Oran, *Combust. Flame* **126**, 1810 (2001)
- S15. A. M. Khokhlov *et al.*, *Astrophys. J.* **524**, L107 (1999)
- S16. D. A. Frank-Kamenetskii, *Diffusion and Heat Transfer in Chemical Kinetics* (Plenum, New York, 1969), chap. 6.
- S17. Ya. B. Zeldovich, G. I. Barenblatt, V. B. Librovich, G. M. Makhviladze, *The Mathematical Theory of Combustion and Explosions* (Consultants Bureau, New York and London, 1985), chap. 4.
- S18. F. A. Williams, *Combustion Theory* (Benjamin-Cummings, Menlo Park, ed. 2, 1985), chap. 5.
- S19. F. X. Timmes, S. E. Woosley, *Astrophys. J.* **396**, 649 (1992)
- S20. A. M. Khokhlov, E. S. Oran, J. C. Wheeler, *Astrophys. J.* **478**, 678 (1997)
- S21. K. Nomoto, D. Sugimoto, S. Neo, *Astrophys. Space Sci.* **39**, L37 (1976)
- S22. J. C. Niemeyer, S. E. Woosley, *Astrophys. J.* **475**, 740 (1997)
- S23. W. Hillebrandt, J. C. Niemeyer, *Annu. Rev. Astron. Astrophys.* **38**, 191 (2000)
- S24. A. M. Khokhlov, E. S. Oran, J. C. Wheeler, *Combust. Flame* **105**, 28 (1996)
- S25. E. Livne, *Astrophys. J.* **406**, L17 (1993)
- S26. D. Arnett, E. Livne, *Astrophys. J.* **427**, 315 (1994)